Journal of Materials Science & Technology 36 (2020) 70–78

Contents lists available at ScienceDirect

Journal of Materials Science & Technology

journal homepage: www.jmst.org

Research Article

Ultralight three-dimensional, carbon-based nanocomposites for thermal energy storage

Oluwafunmilola Ola[a,*], Yu Chen[a], Qijian Niu[b], Yongde Xia[a], Tapas Mallick[a], Yanqiu Zhu[a]

[a] College of Engineering, Mathematics and Physical Sciences, University of Exeter, EX4 4QF, United Kingdom
[b] Key Laboratory of Carbon Fiber and Functional Polymers, Ministry of Education, Changzhou Institute of Advanced Materials Research, Beijing University of Chemical Technology, Beijing, 100029, China

ARTICLE INFO

Article history:
Received 9 May 2019
Received in revised form 29 May 2019
Accepted 15 June 2019
Available online 9 August 2019

Keywords:
Nanocomposites
Foam
Thermal properties
Compressive properties

ABSTRACT

Polymer based nanocomposites consisting of elastic three-dimensional (3D) carbon foam (CF), paraffin wax and graphene nanoplatelets (GNPs) have been created and evaluated for thermal energy storage. The ultralight, highly porous (~98.6% porosity), and flexible CFs with densities of 2.84–5.26 mg/cm^3 have been used as the backbone skeleton to accommodate phase change wax and nanoscale thermal conductive enhancer, GNP. Low level of defects and the ordered sp^2 configuration allow the resulting CFs to exhibit excellent cyclic compressive behavior at strains up to 95%, while retaining part of their elastic properties even after 100 cycles of testing. By dispersing the highly conductive GNP nanofillers in paraffin wax and infiltrating them into the flexible CFs, the resultant nanocomposites were observed to possess enhanced overall thermal conductivity up to 0.76 W/(m K), representing an impressive improvement of 226%, which is highly desirable for thermal engineering.

1. Introduction

Latent heat based thermal energy storage (LHTES) using organic phase change materials (PCM) has the potential to support the system balancing energy generation, demand and supply, thus contributing to the carbon footprint management via achieving an improved overall efficiency. Organic PCMs are used for a wide range of applications in waste heat recovery, solar energy systems, domestic, district and industrial heat and cold storage systems, because they possess advantages such as high energy storage density and low temperature variation during charging and discharging [1,2]. Due to the excellent chemical and thermal stability at temperatures below 500 °C during the charge/discharge cycle, organic PCMs, particularly paraffin wax, have been intensively studied for LHTES applications at low to medium temperature ranges. Other features of PCMs, including low vapor pressure, high latent heat of fusion, small supercooling, low cost, and noncorrosive, are also highly desirable properties for LHTES [3]. Conversely, paraffin wax has several inherent limitations, e.g. low thermal conductivity, rapid volume expansion during phase change and flammability, which limits its practical applicability [4]. Efforts of introducing special forms of encapsulation have been attempted to maintain a stable shape during phase change and prevent leakage to the external environment. To develop high performance PCM nanocomposites, several factors such as thermal conductivity, specific heat capacity, cost and operating temperature range for specific applications must be taken into consideration. The concept of nanocomposites can be applied to overcome these limitations, because nanocomposites offer advanced multi-functionalities than their individual phases. Other approaches include the insertion of different non-metallic and metallic configurations in the form of fins, sheets and tubes into the PCM matrix [5,6]. Although these configurations have been reported to improve the thermal conductivity, they are prone to irreversible defects at elevated temperatures, might not offer long-term chemical stability, and are generally heavy and costly for these storage systems [7,8].

The dispersion of high conductivity nanoparticles especially carbon allotropes can also increase the overall thermal performance, due to their high thermal conductivity, good thermal stability, wettability and corrosion resistance. Several studies have been reported by using graphene nanoplatelets (GNPs) [9], multi-walled carbon nanotubes [10], carbon nanofibers [11] and graphite [12]. Other strategies which include the mixing of PCM with supporting materials such as clay minerals, styrene-butadiene-styrene copolymer and high-density polyethylene, to facilitate high dispersion and shape stabilization, thus preventing leakage of the polymer

---

[*] Corresponding author.
E-mail address: O.Ola@exeter.ac.uk (O. Ola).

https://doi.org/10.1016/j.jmst.2019.06.014

matrix from the TES systems during phase change, have also been documented [13,14].

Hierarchically porous polymers with combined properties of light weight, good flexibility and high absorption capacity can offer numerous possibilities for the development and utilization of nanocomposites in applications ranging from catalysis to environmental remediation [15,16]. Recently, a new class of porous carbon foams (CFs) have been applied to environmental remediation and thermal energy storage due to their ease of regeneration and reuse [17,18]. Utilizing nanocomposites comprising of these 3D porous, flexible CFs with conductive nanofillers can be an effective strategy, as this would allow for simultaneously enhancing the thermal conductivity and mechanical stability of the TES system during repeated heating and cooling cycles, while reducing the size and weight.

In this work, new nanocomposites comprised of CFs prepared from melamine foams, GNPs and paraffin wax as the supporting shape stabilizing material (SM), performance enhancement material (PEM) and organic based PCM, respectively, were investigated for thermal management. The effect of GNP contents on the thermal conductivity of these nanocomposites was further evaluated. This nanocomposite strategy of using these class of porous CFs offers enormous potential to address the barriers of cost, size, weight and cyclic duration that currently limit the wider commercialization of TES.

2. Experimental

Foams made up of melamine-formaldehyde sodium bisulfite copolymer framework (MFs) with a thickness of 25 mm were used as received (Avocation Ltd). A one-step carbonization of MF in an Ar atmosphere at different temperatures led to the CFs. According to the carbonization temperature, the resulting CFs were named, such as CF-800 and CF-1200 referring to samples obtained at 800 °C and 1200 °C, respectively. The nanocomposite was prepared using the CFs, paraffin wax and GNPs. The paraffin wax (Sigma Aldrich, *m.p.* 53–57 °C) was selected as the latent heat storage material for all experiments. Commercial GNPs (abcr GmbH), as the PEM, were first added at different fractions of up to 5 wt% into the melted paraffin wax. Following magnetic mixing and ultrasonic treatment to disperse the GNPs into wax, the molten mixture was then vacuum infiltrated at 200 mbar into the CF, to form the nanocomposites. Vacuum infiltration was carried out using a Buchner funnel with a diameter of 25 mm attached to a rotary vane pump. Upon natural cooling down to 20 °C, the solid nanocomposites were then trimmed to squares of 1 cm × 1 cm, with a thickness of 0.1 cm. The resulting nanocomposites were named according to the GNP content in the paraffin wax, such as CF-1200-2 G referring to nanocomposite containing 2 wt% GNP infiltrated into CFs produced at 1200 °C. Composites of plain wax containing the same amounts of GNPs were also prepared for comparison, against the foam nanocomposites.

Morphological and elemental characterizations of all samples were carried out on a scanning electron microscope with an energy dispersive X-ray spectroscope attachment (SEM-EDX, Hitachi S3200 N, Oxford instrument), operated at 20 kV. TEM experiments were conducted on a JEM-2100 TEM, operated at 200 kV. For the TEM sample preparation, a carbon coated copper grid (300 mesh, Agar) was derived from suspensions containing pieces of foams that were ultrasonically dispersed in ethanol (Sigma Aldrich). The porosity was measured using Micromeritics Autopore IV 9500. Three-dimensional (3D) images of the CFs were recorded with an X-Tek Benchtop 160Xi CT machine. A Renishaw benchtop Raman system, with 532 nm excitation wavelength and 2400 l/mm grating, was used to acquire the Raman spectra of all foams. Powder X-ray diffraction patterns of MFs and CFs were recorded on a Bruker D8 Advance diffractometer (operated at 40 kV, 40 mA), with a CuK_α radiation, at a step size of 0.02° and dwell time of 1 s. Information on the chemical bonding was obtained using Fourier transform infrared spectroscopy (FTIR, Bruker) over a wavelength range of 400 – 4000 cm^{-1}. Thermogravimetric analysis (TGA) was carried out using a TA SDT Q600 instrument, at a ramping rate of 5 °C min^{-1} under Ar atmosphere. Thermal properties were measured on a Mettler Toledo DSC 821e/700 system at a temperature range of 20–80 °C and heating rate of 5 °C/min under N_2 flow. Thermal diffusivity evaluations of the nanocomposites were conducted on a NETZSCH LFA 467 HyperFlash machine. Prior to testing, the 1 cm^2 samples were spray-coated with a thin layer of graphite, to improve the signal to noise ratio and enhance light emission/absorbance during analyses. The thermal conductivity (λ) was extrapolated from the dataset obtained from thermal diffusivities (α), using $\lambda = \alpha\rho C_p$, where ρ and C_p represent the density and specific heat capacity of the sample, separately. An average value was obtained from the software after 3 runs. The cyclic compression test of CFs was carried out on a Lloyds EZ20 advanced universal mechanical testing system, using a 500 N detection cell at a loading rate of 8 mm/min, on a sample of 30 mm × 12 mm × 14 mm.

3. Results and discussion

3.1. Morphology and physicochemical properties of foams

As shown in Fig. 1(a), before carbonization, the MF precursor for CFs has a 3D interconnected porous network, with pore sizes within the range of 90–140 μm. The MF has a density of 8.5 mg/cm^3. After carbonization, the CFs maintain a similar hierarchically porous structure with concave-shaped fibers (Fig. 1(b)–(d)). Depending on the carbonizing temperatures, reductions of up to 95% of the original mass have been recorded for CF-1200 which was subject to the highest carbonization temperature. The resulting CFs are ultralight and flexible, with densities ranging from 2.84 to 5.26 mg/cm^3 which are lower than those reported by several groups [19,20], due to the high porosity of ~98.6%.

In the high magnification image (Fig. 1(b)), nanofibers at the edge of the trusses of sample CF-800 were observed. Nanofibers of a few hundred nm up to mm in length with varying diameters on the edges and surfaces of sample CF-900 were visible (Fig. 1(c)). All truss joints of the CF exhibited an alveoli-shaped structure, whereas the maximum alveoli diameter was observed for the CF-1200 sample. A growth of the alveoli joints must have happened with increased temperatures. Further elemental analyses have shown that the MF is primarily composed of N, C, O and Na in order of increasing amount. The CFs consist of dominantly C and a minute of N, and the maximum C content was recorded for the CF-1200 sample. As shown in Fig. S1, the O/C ratios decrease with increased carbonization temperatures, whilst the N/C ratios rapidly decrease and slightly increase at 1200 °C. Some N in the foam is lost, due to gaseous N_2 and ammonia (NH_3) being released during the carbonization. The microstructure of the CFs was evaluated by using XRD. The broad peaks in the diffraction patterns, as shown in Fig. S2, reveal the feature of microcrystalline domains and low degree of graphitization of the foams.

The diffraction results match well with those of amorphous carbon nitride (g-C_3N_4) synthesized from similar melamine precursors [20,21], of which the 13.1° diffraction peak is indexed to the (100) plane of g-C_3N_4 and the 29.3° peak originates from the (020) plane of g-C_3N_4 which has shifted due to its amorphous nature. In the Raman spectrum, the MF (Fig. 1(e)) shows several intense shifts. The frequencies at 676 and 984 cm^{-1} (marked by M) represent the ring breathing II mode and the in-plane ring breathing I mode of

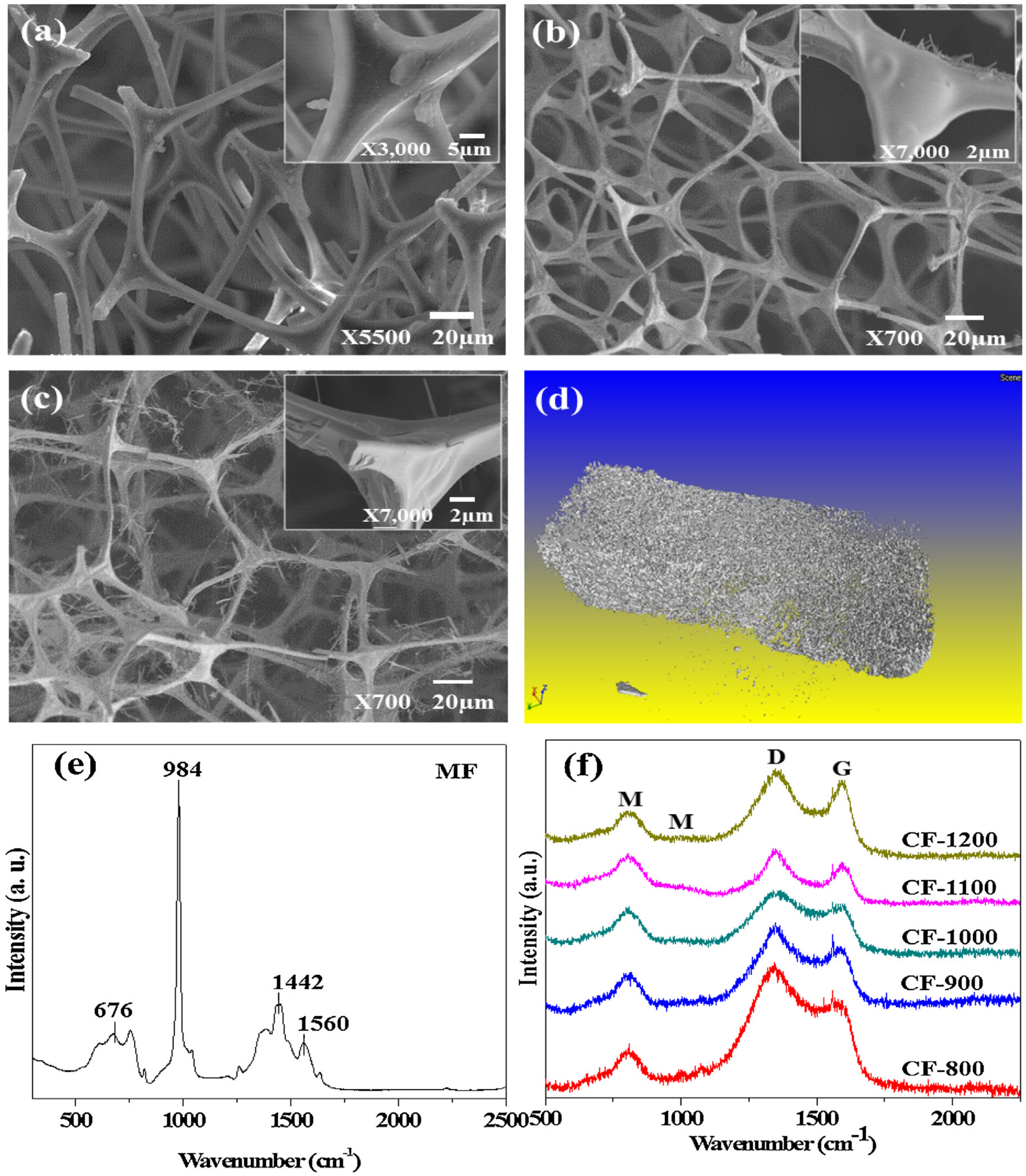

Fig. 1. Morphological and structural characteristics of the MFs and CFs: (a) SEM micrograph of the MF (inset shows the alveoli-shaped joint); (b) SEM micrograph of sample CF-800 (inset showing the presence of nanofibers); (c) SEM micrograph of sample CF-900 (inset showing nanofibers of varying lengths and diameters); (d) Micro-CT image of sample CF-1200; (e) Raman spectrum of the pristine MF; (f) Raman spectra of CFs synthesized at different temperatures.

melamine. The characteristic melamine peak at 676 cm^{-1} is absent in the CFs, due to the substitution of melamine ring upon methylolation [21]. The frequencies lower than 600 cm^{-1} are assigned to the H—N—C–N and N-H$_2$ stretching; whilst the 1442 and 1560 cm^{-1} shifts are due to the out-of-plane C–N stretching.

All CFs possess Raman bands at 804.9–809.1 cm^{-1}, which can be attributed to the out-of-plane N—C–N bending of g-C$_3$N$_4$ [22,23]. Compared with the MF, two new Raman bands appear at 1343–1358 cm^{-1} and 1538–1553 cm^{-1} for the CFs, which can be assigned to the D and G band of carbon. The D band represents the breathing mode in rings originating from disorder-induced carbon; whilst the G band corresponds to the C—C stretching mode in both chains and rings of graphitic carbon. The intensity ratio of the D peak to G peak (I_D/I_G) slightly decreases with increased carbonization temperatures, indicating that lower level of defects has been created and ordering of sp^2 carbon has been initiated at higher temperatures. TEM images of samples CF-800 and CF-1200 show that the CFs are comprised of nanoflakes of various sizes, as shown in Fig. 2(a)–(f). The selected area electron diffraction (SAED) patterns of these samples also confirm that the CFs are mainly amorphous, and that crystallization is being initiated at 1200 °C, as evidenced by the tiny crystalline diffraction spots shown in Fig. 2(f). The TEM results are in good agreement with the Raman spectrum analyses. FTIR spectra of the MF and CFs are shown in Fig. 3(a). Several peaks at 810 and 1455 cm^{-1} are observed for the MF, which correlates to the vibration modes of s-triazine ring, and the peaks at 955, 1530

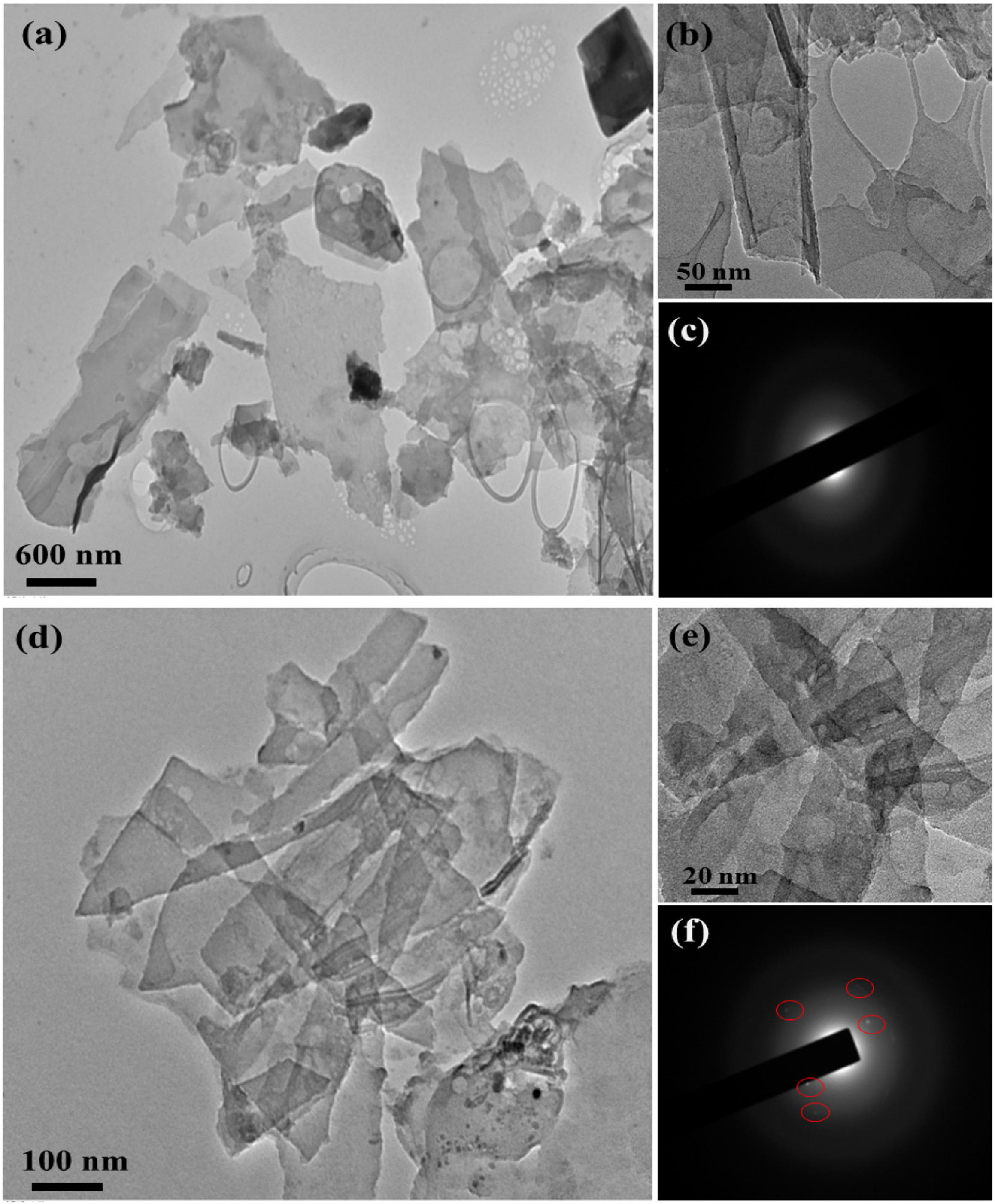

Fig. 2. TEM images and corresponding SAED patterns of (a–c) CF-800 and (d–f) CF-1200. The red circles mark some weak spots indicating crystalline domains.

and 3330 cm^{-1} are linked to the C–H bending, C═N stretching vibration of s-triazine ring and N—H stretching vibration of secondary amine, respectively [24].

For the CFs, absorption is predominantly within the range of 1250 – 2500 cm^{-1}. The absorption peaks at the 1000–1350 cm^{-1} region is due to the C–N stretching. After carbonization, the peak at 810 cm^{-1} that was observed in the MF and CFs of up to 900 °C wanes at higher temperatures. The reduced intensity and disappearance of 810 cm^{-1} adsorption at higher carbonization temperatures have confirmed the initiation of condensation of melamine and rearrangement and/or modification of s-triazine rings. Following thermal condensation of melamine, the appearance of new peaks for all the CFs from C≡N stretching within the range of 2150–2400 cm^{-1} has also been reported linked to this phenomenon [17,25]. Based on the FTIR results, it can be confirmed that the CFs are predominantly made of C–N bonds i.e. C═N and C≡N.

The TGA result in Fig. 3(b) shows that the degradation of the MF under Ar experienced three steps. An initial 5% weight loss before 100 °C can be attributed to the loss of ambient molecular absorptions. The other two sharp decomposition steps occurred at 350 and 620 °C, respectively. The weight loss of 23% at 350 °C can be linked to the sublimation of melamine via the breakdown of methylene bridges or residual methylol groups [24,26]. The foam becomes stable after the final decomposition step after 620 °C and

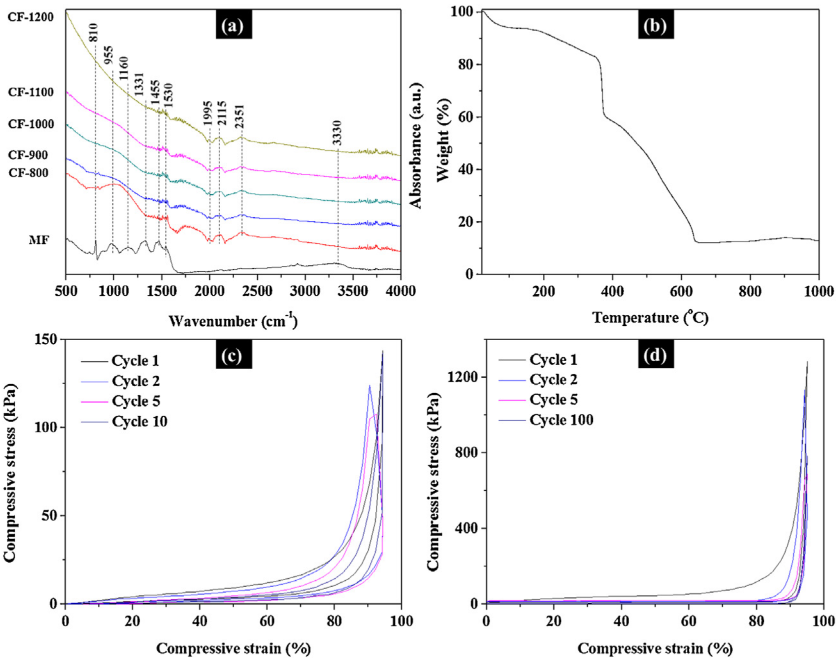

Fig. 3. (a) FTIR spectra of MF and CFs converted at various temperatures, (b) TGA curve of MF in Ar and cyclic compressive behavior of (c) MF and (d) CF-1200 with 95% of strain, tested at a loading rate of 8 mm/min.

retains about 12% of its original weight at 1000 °C. It is possible that the weight loss above 600 °C is due to the breakdown of the triazine rings of melamine. Several groups using in-situ FTIR with TGA analysis have observed the peak disappearance in the FTIR spectra, and they have contributed the weight loss from 600 to 670 °C to the decomposition of volatile organics and triazine rings [24,27].

The mechanical properties of carbon foam are a critical factor for determining its ability to retain excellent shape stabilization while preventing leakage during repeated thermal cycling. The loading and unloading compressive stress–strain curves of the MF and CF-1200 are shown in Fig. 3(c) and (d). The stress-strain curves of CFs are characterized mainly by the elastic and plateau regions which precedes to densification triggered by increased stresses [28]. A large hysteresis between the loading and unloading curves is visible for all samples, which is a typical feature of open cell foams [17]. Both MF and CF-1200 are highly flexible and can tolerate large cyclic strains up to 95%. After unloading, both samples recover most of their volume elastically, and their 3D interconnected porous structure appears to be well-maintained without damage. A maximum compressive strength of ~1275 kPa is observed subject to a strain of 95%, which is larger than any reported values for CFs [28]. After 10 cyclic compression tests at 95% strain, the hysteresis profiles appear to be nearly reproducible, and all unloading curves return to their original state, with a gradual densification occurring after each cycle. After 100 cycles, the peak stress of CF-1200 drops to ~576 kPa, and the unloading stress-strain curve still returns to its initial position, indicating a limited structural damage during the process.

Fig. S3(a)–(d) shows that the intense strain and mechanical densification has contributed to the bending and fracture of some struts by creating a tortuous and densely packed pore structure. A comparison between the samples before and after the cyclic compression has revealed the reduced alignment and order along the fiber strut axis. The plastic deformation was measured to be less than 50% at maximum strain, due to the high structural flexibility and porosity of the CFs. For example, the initial thickness of CF-1200 has decreased by 10% and 48% after the 10th and 100th compression test, respectively. This excellent cyclic behavior of the CFs is highly desirable for stabilizing the SM for it to cope with the dimensional changes caused by heating and cooling. The CF-1200 has demonstrated superior mechanical properties and strength to the MF, with an elastic modulus of 0.86 kPa against 0.22 kPa for the MF.

3.2. Chemical compatibility, shape stability and thermal properties of nanocomposites

Chemical compatibility between PCM and carbon foams were evaluation using FTIR and XRD. Fig. 4(a) shows the FTIR spectra of paraffin wax and nanocomposites with varying amounts of GNPs. Typical absorption bands at 720 and 1378 cm^{-1} correspond to in-plane deformation and symmetric C–H bending absorption of CH_2 and CH_3 groups in the paraffin wax, respectively [29]. Peaks at 1462 and 2848 cm^{-1} can be assigned to the C—H bending vibration and C—H stretching vibration of CH_2, respectively. The C—H stretching vibration of CH_3 can be found at wavenumber of 2915 cm^{-1}. All nanocomposites possess characteristic peaks of paraffin wax which indicate that the nanocomposites are mainly composed of paraffin wax. Since there are no new peaks and additional functional groups belonging to GNP, it can be concluded that chemical interaction between carbon foam, paraffin wax and GNP does not occur that could result in change in molecular structure of the final nanocomposite. As shown in Fig. 4(b), nanocomposites possess similar diffraction patterns to the pure paraffin wax. The (100) and (200) planes of paraffin wax present at 21.7° and 24.3° were observed to decrease in intensity. No other diffraction peaks were observed. The reduced XRD peak intensity clearly indicates that crystallization is impeded by the introduction of paraffin wax into the polymer matrix rather than altering its crystal structure.

Fig. 4(c) shows the typical DSC curves for the heating and cooling cycles of paraffin wax and carbon-based nanocomposites while Table 1 lists the endset crystallization/melting temperatures (T_{CE}/T_{ME}), onset crystallization/melting temperatures (T_{CO}/T_{MO}), peak crystallization/melting temperature (T_{CP}/T_{MP}) and enthalpy of crystallization/melting ($\Delta H_{CC}/\ \Delta H_{MC}$). Two different phase change peaks are observed during each heating and cooling cycle. For pure

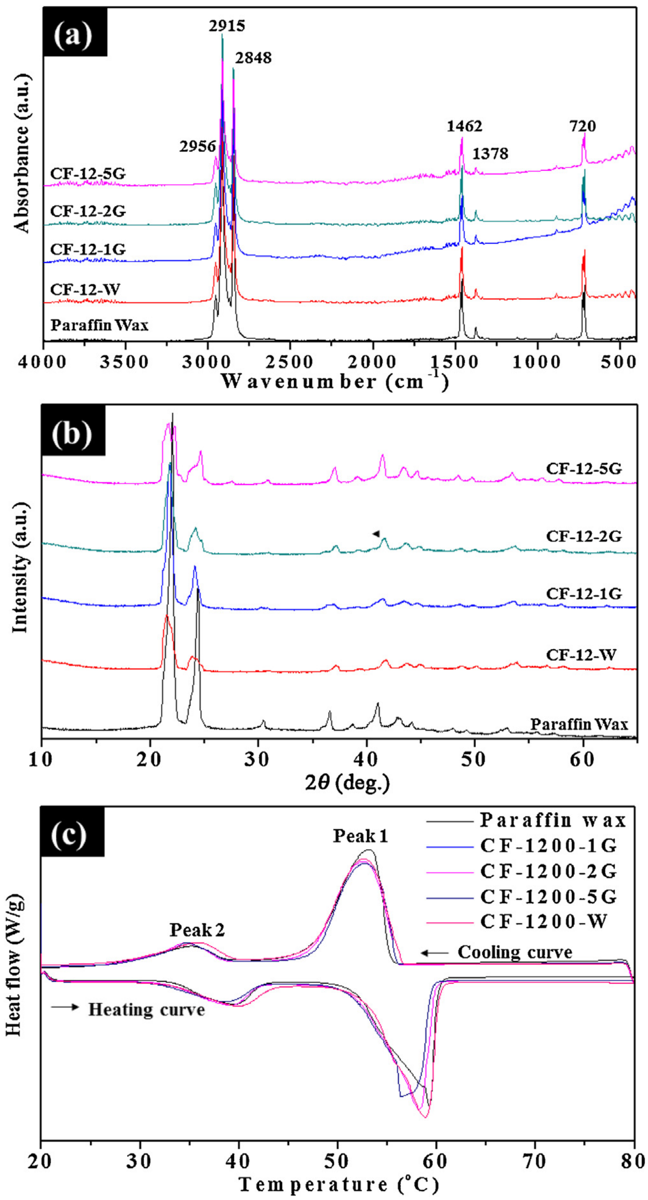

Fig. 4. (a) FTIR spectra, (b) XRD patterns, and (c) DSC heating and cooling curves of paraffin wax and its nanocomposites.

wax, the primary and secondary peaks at higher and lower temperatures are linked to the solid–liquid phase transition and solid–solid phase transition, respectively. During melting, two peaks appear at ~36 °C and ~53 °C, which shift to ~40 °C and ~59 °C during solidification. The introduction of wax and of GNP altered the phase transition temperatures of the nanocomposites during both melting and crystallization compared with the paraffin wax. The melting temperature of paraffin wax slightly decreased from 53.5 °C to 53.1 °C with increasing the GNP fraction, then marginally increased. A similar decreasing trend also occurred during crystallization.

This phenomenon can be accounted for by the GNP initiating steric hindrance in the paraffin wax [11]. Due to the confinement effect of the paraffin wax together with GNPs in the pores of CF, the solidification temperature of paraffin wax could be lowered/decreased. The observed slight decrease of melting points may be due to the existence of high concentration of GNPs deposited on the external surface of CFs rather than being confined in the pores of CFs [30]. The latent enthalpy was estimated by numerical integration of the total area under the peaks. The crystallization enthalpies of the nanocomposites calculated from Fig. 4(c) shows a 6.9% decrease against the paraffin wax. A slight increase in the melting enthalpy is observed for the CF-1200-1 G sample, and then decreases with increasing the fraction of GNPs. The enthalpy change can be linked to the inference of GNPs with nucleation which can also be confirmed from the XRD results which shows that GNPs slightly altered the crystallinity of the paraffin wax. Since there is no chemical reaction amongst individual components of the nanocomposite, the phase change enthalpies of the nanocomposites could be slightly lowered due to the replacement of some paraffin wax with GNP and the free movement of paraffin being reduced in the 3D polymer matrix.

Shape stability is critical for evaluating the performance of PCM leakage during repeated thermal cycling. The shape stability was evaluated by heating up the nanocomposites to defined temperatures of 30–90 °C on a hot stage for 5 min which was observed via digital photography. As shown in Fig. 5, all samples maintain defined shapes and remain in the solid state below the melting point of paraffin wax. Above the PCM melting point, pure paraffin wax changes from solid to liquid state while the other nanocomposites remain intact without any observed leaks. Further temperature increases to 90 °C result in a complete transformation of the PCM to a liquid state. PCM remains trapped in the 3D structure of nanocomposites via strong capillary forces which hold the PCM within the polymer matrix. The nanocomposites maintain good shape stability due to the mechanical integrity of the flexible network structures of the carbon foam which allow them to cope with the volume changes during repeated thermal cycling. The correlation between shape stabilization and wettability of the components in the nanocomposites will be evaluated in the future as a means of improving the stability and thermal properties of the nanocomposites.

Thermal conductivity of nanocomposites prepared with wax only (without GNPs) was measured at a temperature range of −50 °C to 40 °C, and the results are shown in Fig. 6(a). With increased carbonization temperatures, the thermal conductivity increases, exhibiting a 70% maximum improvement for the CF-1200 sample against paraffin wax which values at 0.23 W/(m K). All samples including paraffin wax also show a decreasing trend with increased testing temperatures.

It is obvious that higher carbonization temperature leads to more carbon content in the foam, as evidenced by the SEM-EDS analyses that CF-1200 has a maximum carbon content of 60.03% which converts to a carbon yield of 6.5%. The higher carbon con-

Table 1
DSC heating and cooling characteristics of paraffin wax and nanocomposites.

Sample	T_{CO} (°C)	T_{CE} (°C)	T_{CP} (°C)	ΔH_{CC} (J/g)	T_{MO} (°C)	T_{ME} (°C)	T_{MP} (°C)	ΔH_{MC} (J/g)
Wax	55.29	47.40	53.49	126.24	55.99	60.07	58.81	127.56
CF_12_W	55.13	45.32	51.70	122.04	52.33	61.62	57.52	125.28
CF_12_1G	56.26	47.43	53.15	126.00	53.70	60.19	58.11	131.52
CF_12_2G	56.54	48.00	53.45	126.72	55.20	59.97	58.00	126.12
CF_12_5G	55.94	47.77	53.05	117.48	54.89	59.42	55.98	118.20

T_{CO}/T_{MO}: onset crystallization/melting temperatures; T_{CE}/T_{ME}: endset crystallization/melting temperatures; T_{CP}/T_{MP}: peak crystallization/melting temperature; $\Delta H_{CC}/\ \Delta H_{MC}$: enthalpy of crystallization/melting; DSC measurement uncertainty: ±2%.

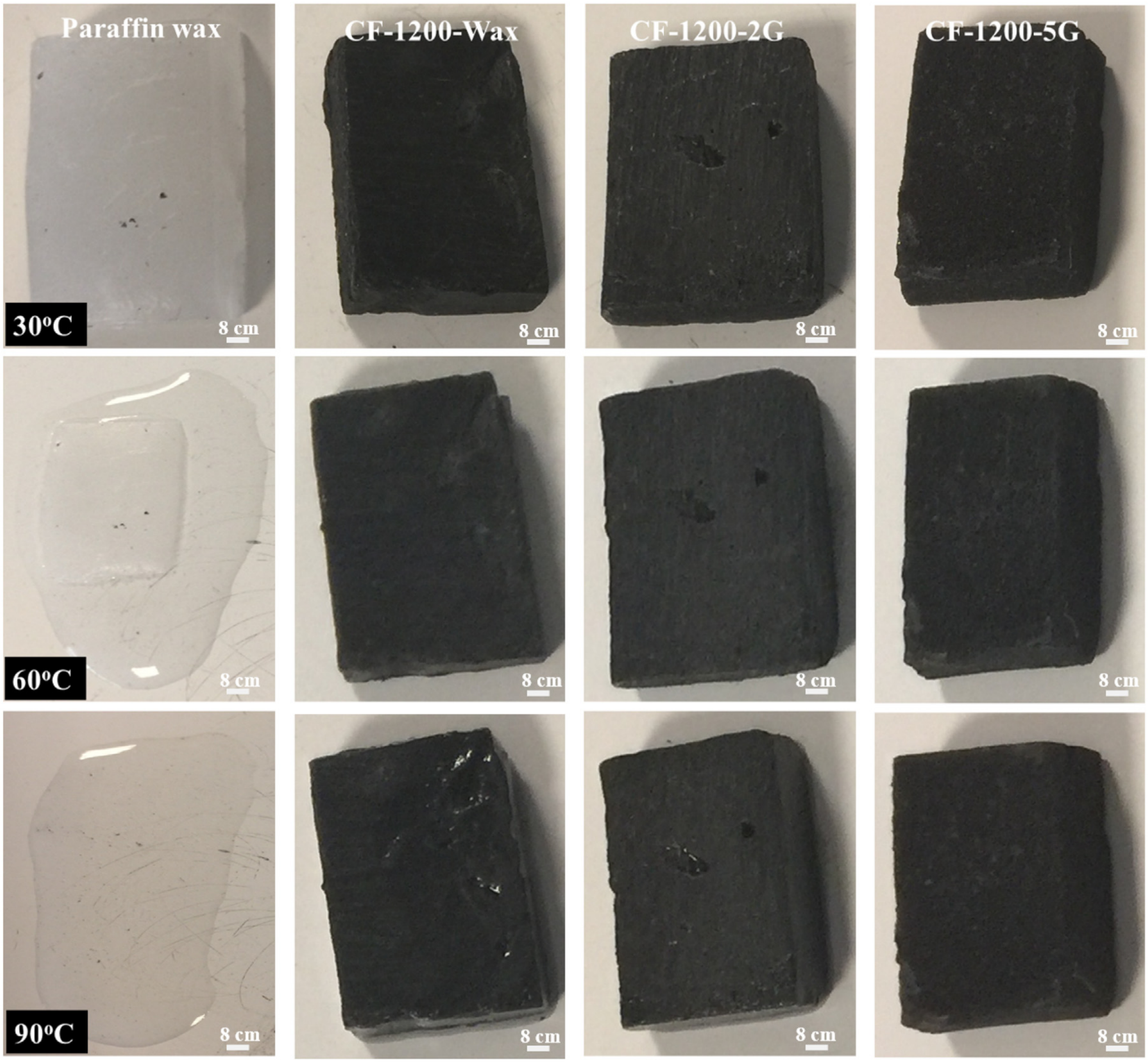

Fig. 5. Shape stability studies of the PCM mix and different carbon foam nanocomposites.

tent and better graphitization degree are believed to be the reason for the carbonization temperature correlation to the thermal conductivity.

The influence of GNP filler contents on the thermal conductivity of different nanocomposites is shown in Fig. 6(b). For nanocomposites prepared using wax and 2 wt% GNP nanofiller, the thermal conductivity increases progressively, with maximum values observed for the CF-1200 sample. This also confirms the contributing role that the increased carbon content played in increasing thermal conductivity. The effect of different fractions of GNP up to 5 wt% was further studied on CF-1200 at the same temperature range. As shown in Fig. 6(c), the nanofiller contents strongly influence the thermal conductivity, with sample CF-1200-5 G showing an optimal improvement of 226%, whilst CF-1200-2 G and CF-1200-1 G show 127 and 43% improvements, compared with wax and other samples. The above results have confirmed the key role of the CFs in thermal conductivity improvement. Although GNPs have been reported to have very high thermal conductivities up to 3000 W/(m K) [31], the low fraction of GNP in the composites could not form an interlinked network to exhibit the theoretical improvement. However, the 226% increase in the CFs composites is still very impressive. Meanwhile, the as-synthesized CF-1200-5 G has a lower thermal conductivity compared with other metal and graphite foam/PCM composites reported in the literature [18,32,33]. This is due to the presence of high-quality graphitic carbon used in their nanocomposite formulation. Our Raman studies have confirmed that the foams utilized in this study possess mainly amorphous rather than graphitic carbon network (Fig. 1(f)).

The thermal stability of the PCM mix and carbon foam nanocomposites was evaluated using TGA, and the results are shown in Fig. 6(d). Pure paraffin wax starts decomposing at *ca.* 250 °C. Nanocomposites possess similar degradation pattern because they are made up of mainly paraffin wax. The weight loss observed at 290 °C can be linked to paraffin chains being broken down during degradation of volatile organic compounds. The nanocomposites maintain excellent thermal stability since thermal degradation was not observed within their phase change temperatures and thermograms did not shift to lower temperature during the initiation of degradation process. Fig. 7(a) and (b) illustrates the thermal and chemical stabilities of the CF-1200-5 G nanocomposites evaluated over several thermal cycles.

After 100 thermal cycles, the latent heat of crystallization and phase change temperatures remain almost identical to the first cycle, with only slight increases by 2% and 1.9%, respectively. The FTIR spectra of CF-1200-5 G after thermal cycling also confirm the high thermal stability, since existing vibration peaks belonging to the functional groups of paraffin wax were observed. In short, it can be deduced from the DSC and FTIR results that the thermal

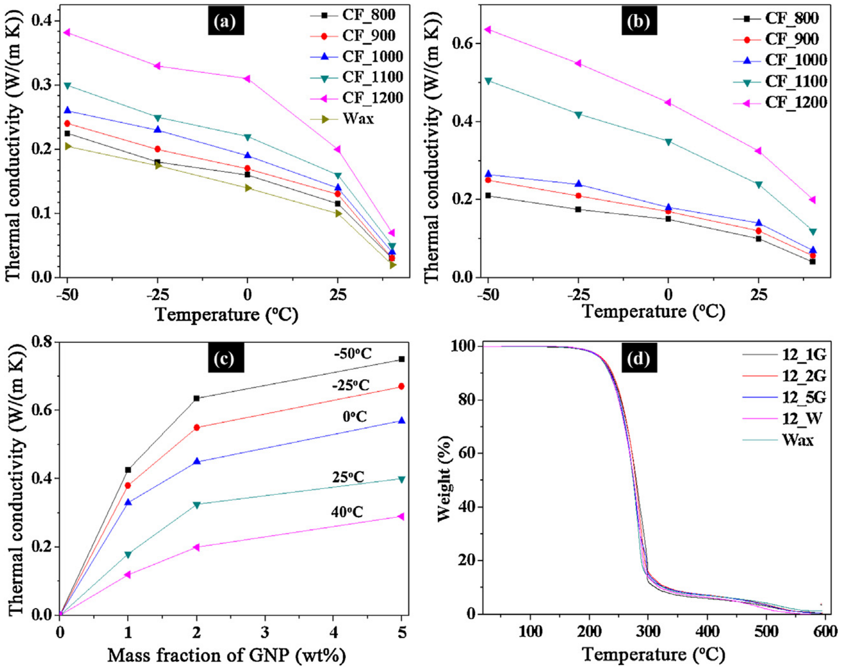

Fig. 6. Thermal properties of paraffin wax and nanocomposites: (a) thermal conductivities of pure wax and nanocomposites prepared with paraffin wax; (b) thermal conductivities of nanocomposites prepared with wax and 2 wt% GNP; (c) thermal conductivities of CF-1200 nanocomposites prepared with different GNP contents; (d) thermogravimetric analysis curves.

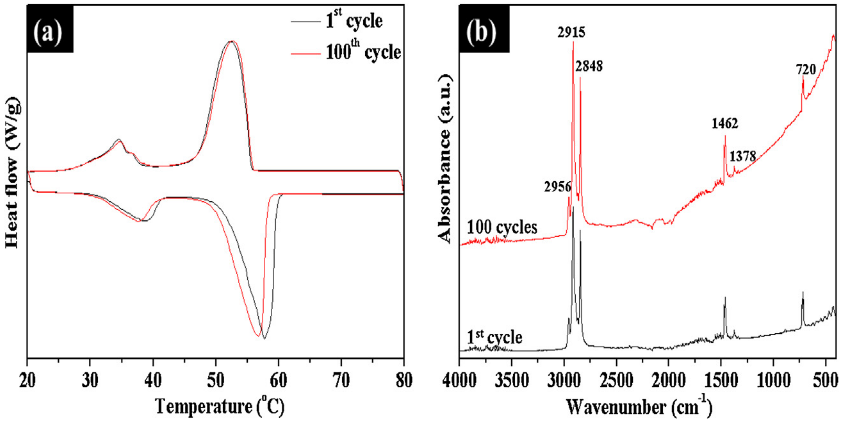

Fig. 7. (a) DSC curves and (b) FTIR spectra of sample CF-1200-5 G after 100 thermal cycles.

properties and chemical structure of CF-1200-5 G did not change after thermal cycles. Due to the excellent shape stabilization, thermal stability and reliability, sample CF-1200-5 G holds considerable promise for improving the performance in space heating applications.

4. Conclusion

PCM-based nanocomposites have been successfully fabricated using chemically compatible components made up of ultralight and highly flexible 3D CFs, paraffin wax and GNPs, as the shape stabilized materials (SM), phase change material (PCM) and performance enhancing material (PEM), respectively. The ultralight CFs created by the one-step carbonization of MFs exhibit excellent thermal and mechanical properties. An optimal 226% improvement in thermal conductivity for the 5 wt% GNP filled PCM nanocomposites in the CFs has been achieved. This work represents a novel, simple, and cost-effective way to fabricate stable, high-performance TES materials that are suitable for energy and environmental applications.

Acknowledgement

This work was supported financially by the Engineering and Physical Sciences Research Council, United Kingdom (Grant No. EP/P003435/1).

Appendix A. Supplementary data

Supplementary material related to this article can be found, in the online version, at doi:https://doi.org/10.1016/j.jmst.2019.06.014.

References

[1] A. Sharma, V.V. Tyagi, C.R. Chen, D. Buddhi, Renew. Sustain. Energy Rev. 13 (2009) 318–345.

[2] S. Sharma, A. Tahir, K.S. Reddy, T.K. Mallick, Sol. Energy Mater. Sol. Cells 149 (2016) 29–39.
[3] R.K. Sharma, P. Ganesan, V.V. Tyagi, H.S.C. Metselaar, S.C. Sandaran, Energy Convers. Manage. 95 (2015) 193–228.
[4] Y. Zhang, X. Zheng, H. Wang, Q. Du, J. Mater. Chem. A 2 (2014) 5304–5314.
[5] R. Velraj, R.V. Seeniraj, B. Hafner, C. Faber, K. Schwarzer, Sol. Energy 65 (1999) 171–180.
[6] H.M. Ettouney, I. Alatiqi, M. Al-Sahali, S.A. Al-Ali, Renew. Energy 29 (2004) 841–860.
[7] Z. Ge, F. Ye, Y. Ding, Chemsuschem 7 (2014) 1318–1325.
[8] Z. Zhang, N. Zhang, J. Peng, X. Fang, X. Gao, Y. Fang, Appl. Energy 91 (2012) 426–431.
[9] J. Xiang, L.T. Drzal, Sol. Energy Mater. Sol. Cells 95 (2011) 1811–1818.
[10] F. Ye, Z. Ge, Y. Ding, J. Yang, Particuology 15 (2014) 56–60.
[11] L.W. Fan, X. Fang, X. Wang, Y. Zeng, Y.Q. Xiao, Z.T. Yu, X. Xu, Y.C. Hu, K.F. Cen, Appl. Energy 110 (2013) 163–172.
[12] M. Li, Appl. Energy 106 (2013) 25–30.
[13] Y. Cai, Q. Wei, F. Huang, S. Lin, F. Chen, W. Gao, Renew. Energy 34 (2009) 2117–2123.
[14] S.G. Jeong, S.J. Chang, S. We, S. Kim, Sol. Energy Mater. Sol. Cells 139 (2015) 65–70.
[15] X. Huang, X. Chen, A. Li, D. Atinafu, H. Gao, W. Dong, G. Wang, Chem. Eng. J. 356 (2019) 641–661.
[16] M.M. Umair, Y. Zhang, K. Iqbal, S. Zhang, B. Tang, Appl. Energy 235 (2019) 846–873.
[17] A. Stolz, S. Le Floch, L. Reinert, S.M.M. Ramos, J. Tuaillon-Combes, Y. Soneda, P. Chaudet, D. Baillis, N. Blauchard, L. Duclaux, A. San-Miguel, Carbon 107 (2016) 198–208.
[18] H. Ji, D.P. Sellan, M.T. Pettes, X. Kong, J. Ji, L. Shi, R.S. Ruoff, Energy Environ. Sci. 7 (2014) 1185–1192.
[19] X. Gui, J.Q. Wei, K.L. Wang, A.Y. Cao, H.W. Zhu, Y. Jia, Q.K. Shu, D.H. Wu, Adv. Mater. 22 (2010) 617–621.
[20] Z.P. Chen, W.C. Ren, L.B. Gao, B.L. Liu, S.F. Pei, H.M. Cheng, Nat. Mater. 10 (2011) 424–428.
[21] M.L. Scheepers, R.J. Meier, L. Markwort, J.M. Gelan, D.J. Vanderzande, B.J. Kip, Vibr. Spectrosc. 9 (1995) 139–146.
[22] L. Stagi, D. Chiriu, A. Ardu, C. Cannas, C.M. Carbonaro, P.C. Ricci,J. Appl. Phys. 118 (2015), 125502.
[23] M. Prabhaharan, A.R. Prabakaran, S. Gunasekaran, S. Srinivasan, Spectrochim. Acta A. 123 (2014) 392–401.
[24] D.J. Merline, S. Vukusic, A.A. Abdala, Polym. J. 45 (2012) 413–419.
[25] A.C. Ferrari, S.E. Rodil, J. Robertson,Phys. Rev. B 67 (2003), 155306.
[26] H. Yan, Y. Chen, S. Xu, Int. J. Hydrogen Energy 37 (2012) 125–133.
[27] L. Costa, G. Camino, J. Therm. Anal. 34 (1988) 423–429.
[28] S.K. Reddy, D.B. Ferry, A. Misra, RSC Adv. 4 (2014) 50074–50080.
[29] S.Y. Wu, X. Tong, C.D. Nie, D.Q. Peng, S.G. Gong, Z.Q. Wang, J. Therm. Anal. Calorim. 124 (2016) 181–188.
[30] L. Xia, P. Zhang, R.Z. Wang, Carbon 48 (2010) 2538–2548.
[31] H.S. Kim, H.S. Bae, J. Yu, S.Y. Kim, Sci. Rep. 6 (2016) 26825.
[32] Y. Li, J. Li, Y. Deng, W. Guan, X. Wang, T. Qian, Appl. Energy 171 (2016) 37–45.
[33] M.T. Pettes, H. Ji, R.S. Ruoff, L. Shi, Nano Lett. 12 (2012) 2959–2964.